High-throughput *in vivo* vertebrate screening

Carlos Pardo-Martin[1–3,5], Tsung-Yao Chang[1,5], Bryan Kyo Koo[1], Cody L Gilleland[1], Steven C Wasserman[4] & Mehmet Fatih Yanik[1,4]

We demonstrate a high-throughput platform for cellular-resolution *in vivo* chemical and genetic screens on zebrafish larvae. The system automatically loads zebrafish from reservoirs or multiwell plates, and positions and rotates them for high-speed confocal imaging and laser manipulation of both superficial and deep organs within 19 s without damage. We performed small-scale test screening of retinal axon guidance mutants and neuronal regeneration assays in combination with femtosecond laser microsurgery.

Small size, optical transparency of complex organs and ease of culture make the zebrafish (*Danio rerio*) larva an ideal organism for large-scale *in vivo* genetic and chemical studies of many processes that cannot be replicated *in vitro*. Zebrafish models of several human diseases have been developed[1–5]. Lead compounds discovered by screening chemical libraries for efficacy in zebrafish disease models have been useful for pharmaceutical discovery owing to the high level of conservation of drug activity between humans and zebrafish[1–5].

Visualizing most zebrafish organs requires manipulating and properly orienting the larvae. Even with confocal or two-photon microscopy, optical access is often impeded by pigmentation, by intervening organs such as eyes and heart or by the highly autofluorescent yolk sac. Current methods to address these challenges involve treatment with the toxic chemical phenylthiourea to suppress pigmentation[6], manually transferring zebrafish from multiwell plates or reservoirs and manually orienting them in viscous media such as agar. These processes are too slow and unreliable for high-throughput screens. Molded agar plates can also be used to orient zebrafish[7]. However, this is also a relatively coarse process, and it can be done rapidly only for the lateral orientation, whereas imaging many organs (such as brain) requires other orientations. The thick agar molds also prevent high-resolution three-dimensional microscopy and optical manipulations. To improve the throughput and complexity of zebrafish screens, we developed the vertebrate automated screening technology (VAST) that automatically manipulates and images zebrafish at cellular resolution in three dimensions (**Fig. 1** and Online Methods).

Each cycle of VAST includes the following steps: loading, detection, positioning, rotation, focusing, imaging, laser manipulation and dispensing. Such capabilities enable both genetic and pharmaceutical cellular-resolution whole-organism screens[8] (**Supplementary Fig. 1**). During loading, the system extracts larvae either from a multiwell plate or a reservoir. A high-speed photodetection system composed of a photodiode and two LEDs

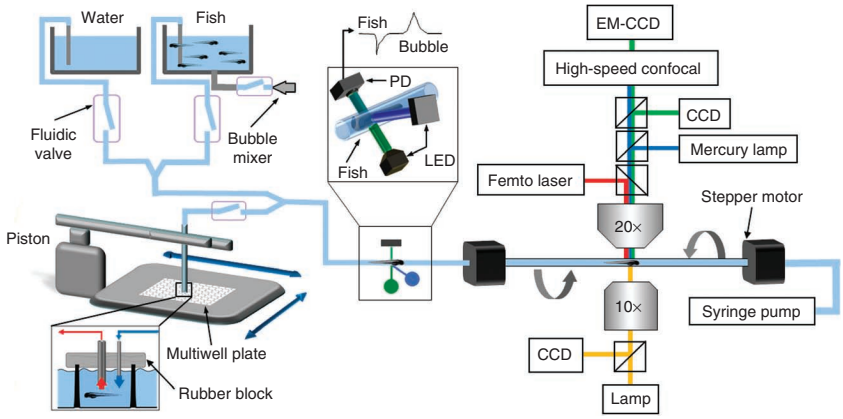

Figure 1 | Schematic of zebrafish manipulation and imaging platform. Larvae are automatically loaded to the system from either reservoirs or multiwell plates. Reservoirs are connected to the system via fluidic valves and a bubble mixer prevents the larvae from settling. The multiwell plate is located on a motorized *x*–*y* stage, which positions individual wells below larva-loading (red arrow) and water-supply (blue arrow) tubes, both held by a silicone rubber block. The block seals the well surfaces as a piston moves the tubes into the wells. A photodetection system including two LEDs and one high-speed photodiode (PD) discriminates the passage of a larva from air bubbles and debris. Two stepper motors hold a capillary along its axis of rotation; this assembly is mounted on a three-axis position stage (not shown) and held between an upright microscope for confocal imaging and an inverted microscope for brightfield imaging. A multifocal confocal head with a cooled electron-multiplying charge-coupled device (CCD) camera and a second large-area CCD connected to the upright port are used for high-speed confocal and widefield fluorescence imaging. A high-speed CCD camera connected to the inverted port allows rapid brightfield detection and positioning of larvae. A femtosecond laser beam used for microsurgery is directed to the upper beam path by a dichroic filter and focused on the sample through the objective.

[1]Department of Electrical Engineering and Computer Science, Massachusetts Institute of Technology (MIT), Cambridge, Massachusetts, USA. [2]School of Engineering and Applied Sciences, Harvard University, Cambridge, Massachusetts, USA. [3]Division of Health Sciences and Technology, MIT, Cambridge, Massachusetts, USA. [4]Department of Biological Engineering, MIT, Cambridge, Massachusetts, USA. [5]These authors contributed equally to this work. Correspondence should be addressed to M.F.Y. (yanik@mit.edu).

RECEIVED 11 JANUARY; ACCEPTED 14 JUNE; PUBLISHED ONLINE 18 JULY 2010; DOI:10.1038/NMETH.1481

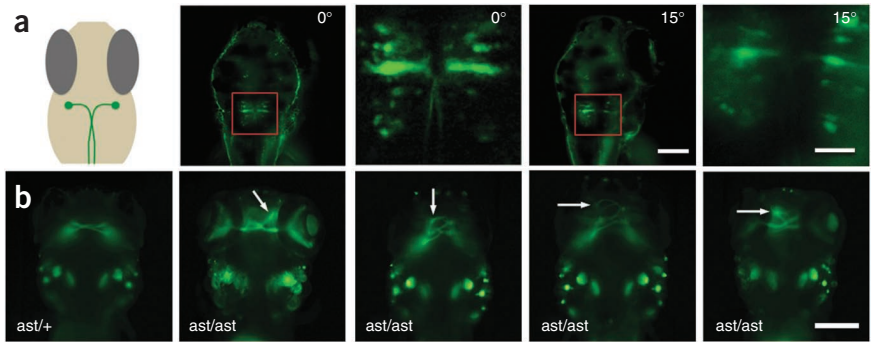

Figure 2 | Orientation, imaging and screening of zebrafish larvae. (**a**) Schematic showing the midline crossing of Mauthner axons (left) and confocal images of GFP-expressing Mauthner cells at 0° and 15° (right). Magnified versions of boxed areas are shown to the right of each image. (**b**) Widefield fluorescence images illustrating the phenotypes distinguished in a small-scale test screen. Representative images showing GFP-labeled axons of retinal ganglion neurons projecting to the optic tectum in larvae of the indicated genotypes. Arrows point to the misguided projections. Scale bars, 150 µm (50 µm in magnified images in **a**).

discerns the entry of larvae into the loading tube. The photodiode senses transmitted light from one LED and scattered light from the other LED. By simultaneously monitoring both the transmission and scattering signals, the system discriminates larva from air bubbles and debris with 100% reliability (n = 1,000). After loading and photodetection, the larva moves from the larger loading tube into a capillary[9,10] positioned in the field of view of an optical imaging and manipulation system. The capillary has a refractive index similar to that of water, allowing the use of high-numerical-aperture water-immersion objectives. Using a fast camera and an automated image-processing algorithm, the syringe pump coarsely positions the larva. Next, a three-axis stage automatically moves the capillary assembly to precisely position the larva's head at the center of the field of view. Two stepper motors then orient the larva. Thus, larvae can be positioned and oriented to allow access from any angle. They can also be rapidly reoriented, allowing visualization of organs from multiple angles. At the end of the cycle, larvae can be dispensed back into either individual wells or larger containers by executing the loading process in reverse (Online Methods and **Supplementary Fig. 2**).

Larvae are imaged through two objective lenses: an upright, high-resolution water-immersion objective and an inverted air objective. This allows both widefield fluorescence imaging and high-resolution confocal microscopy. Imaging most phenotypes requires larvae to be oriented at specific angles. For instance, the midline crossing of the Mauthner motor neuron axons that project into the spinal cord is visible only when directly observed from the hindbrain (**Fig. 2a**). At less favorable orientations, this structure is obscured. We performed a small-scale test screen on zebrafish with a similar midline-crossing phenotype, the midline crossing of retinal axon projections to the optic tectum (**Fig. 2b** and **Supplementary Fig. 3**). Screening for retinal axon misguidance mutants had previously led to the discovery of *astray* mutant alleles in the *robo2* gene[11]. Homozygous *robo2*$^{ti272z/ti272z}$ (ast/ast) zebrafish do not exhibit proper midline crossing, but the projections are normal in heterozygous *robo2*$^{ti272z/+}$ (ast/+) zebrafish. Using our system, we could distinguish wild-type larvae from *robo2* mutants[12] with a sensitivity of 100% and specificity of 98.8% for a 96-well plate with 83 randomly seeded mutants. The 1.20% false negative error in identification of ast/ast zebrafish was due to the rare cases of mutants with strong phenotypic similarity to the wild type. The system could thus be used for large-scale chemical screens for small molecules that rescue such misguidance.

In conjunction with sample positioning and orientation, VAST also allows *in vivo* optical manipulations such as localized activation of fluorescent reporters and ion channels, uncaging of compounds and femtosecond laser microsurgery[13] with subcellular precision. We used this system to monitor neuronal regeneration[14] after injury by laser microsurgery[15] (**Fig. 3a**). The lateral-neuron axon fiber bundle projecting along the trunk of a larva is visible when the larva is laterally oriented. We axotomized the bundle by focusing near-infrared femtosecond laser pulses using the following semiautomated process. A user selected a cell body by clicking on a graphical user interface; an algorithm then measured the user-specified distance from the cell body to the point of axotomy along the axon; and the position stage automatically moved the selected axonal region to the focal spot of the laser for axotomy. We imaged regenerating axonal fibers at 18 h and 24 h after axotomy (**Fig. 3a**). The laser pulses were delivered with high precision (1.7 µm)[13], and the subsequent response of the tissue to the laser (immediate retraction of nerve fibers) showed some variability, leading to a distribution of cut sizes (8.1 ± 5.5 µm (± s.d., n = 30); **Fig. 3b**). All zebrafish recovered from surgery within 30 min with no apparent morphological abnormality, and 100% of the zebrafish survived 24 h after surgery (n = 30).

A complete cycle of loading, positioning, cellular-resolution imaging and dispensing a zebrafish took less than 16 s (**Table 1**). Axotomy required an additional 2.1 s on average. Screening an entire multiwell plate took 31.85 min with an average of 19.9 s per well, which included the additional interval for retracting, moving

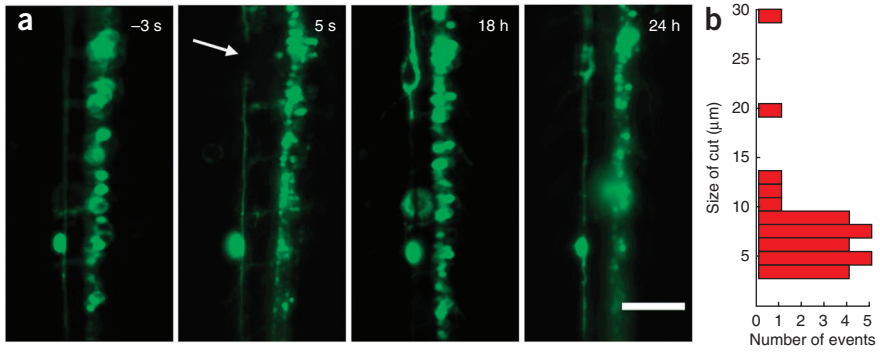

Figure 3 | Laser microsurgery and neuronal regeneration. (**a**) Widefield fluorescence images of enhanced GFP (EGFP)-expressing lateral-neuron axon fibers in a 3-d.p.f. larva are shown at the indicated times before and after axotomy. Scale bar, 75 µm. (**b**) Distribution of laser cut sizes (n = 30).

Table 1 | Average duration of screening steps

Step	Time ± s.d.[a] (s)
Loading from multiwell plate	2.1 ± 0.4
Loading from reservoir	2.2 ± 0.3
From photodetector to field of view	2.7 ± 0.3
Positioning	2.9 ± 0.6
Orienting and focusing	5.6 ± 1.7
Microsurgery	2.1 ± 0.5
Unloading	2.5 ± 0.1

[a]n = 20 for each, except n = 30 for microsurgery.

and inserting the loading apparatus, and sealing the wells. Zebrafish could also be loaded and imaged multiple times for time-lapse assays. Performed manually, assays of similar complexity require about 10 min per zebrafish, and the assays are error-prone.

Zebrafish larvae are delicate and particularly susceptible to injury by tearing at sharp edges or by deformation. The most substantial potential for damaging larvae occurred as they entered the loading tube at the high aspiration rates needed to achieve the desired throughput. To lessen this risk, we started the flow at a low initial rate and increased it at an acceleration of 42 µl s^{-2} until a larva was detected by the high-speed photodetector. The maximum flow rate was limited to 330 µl s^{-1}. At this maximum rate, no injury occurred while larvae were traveling in the tubing. After a larva was detected by the photodetector, the control software decreased the aspiration rate to 83 µl s^{-1} to allow automated recognition of the zebrafish by the camera.

We assessed the health of 450 larvae screened at 2 d post fertilization (d.p.f.) at three different initial aspiration rates (**Fig. 4a**). The assessment was based on both functional and morphological criteria (Online Methods). At all flow rates, heartbeat and touch response matched those of controls. We never observed yolk tearing (n = 450). At the highest initial flow rate of 330 µl s^{-1}, 2% of zebrafish exhibited morphological abnormalities. With a slightly slower initial aspiration rate (increasing the screening time by approximately 1 s), all health criteria matched those of controls (**Fig. 4a**). We measured postmanipulation developmental delay by monitoring the time of appearance of the swimming bladder. There was no significant difference between the development of larvae that were manipulated by the system and control zebrafish (P = 0.94), even at the highest flow rates (**Fig. 4b**). Among the different larval age groups tested (2–7 d.p.f., n > 100 per age), we observed no difference in health.

In summary, we demonstrate a high-throughput vertebrate screening platform with cellular-resolution imaging and manipulation capabilities that should permit large-scale *in vivo* study of complex processes such as organ development, neural degeneration and regeneration, stem cell proliferation, cardiovascular, immune, endocrine and nervous system functions, pathogenesis, cancer and tissue specificity and toxicity of drugs.

METHODS

Methods and any associated references are available in the online version of the paper at http://www.nature.com/naturemethods/.

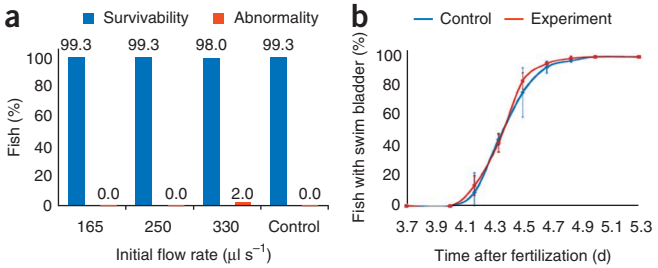

Figure 4 | Quantitative assessment of zebrafish health. (**a**) Survival and abnormality of larvae as a function of initial flow rate (n = 150 for each rate). (**b**) Appearance time of swim bladder in screened and control fish (one way ANOVA, P = 0.94, average of three independent experiments with 50 fish analyzed in each; error bars, s.d.; n = 3).

Note: Supplementary information is available on the Nature Methods website.

ACKNOWLEDGMENTS

We thank the following funding sources: US National Institutes of Health Director's Innovator award (1-DP2-OD002989–01), Packard award in Science and Engineering, Alfred P. Sloan award, Sparc Grant from the Broad Institute, National Science Foundation Fellowship, Foxconn Sponsorship and the "La Caixa" Graduate Fellowship. We thank A. Amsterdam and N. Hopkins (MIT), and A. Schier and I. Woods (Harvard University) for the fluorescent lateral neuron line; C. Chien (University of Utah) for the fluorescent retinal ganglion line (*robo2*$^{ti272z/ti272z}$ with *Tg(pou4f3:gap43-GFP)s356t*)[10,11]; and S. Johnson (Washington University at St. Louis) and R. Jain and M. Granato (University of Pennsylvania) for the fluorescent Mauthner line *Et(tol2:GFP) j1282b*.

AUTHOR CONTRIBUTIONS

C.P.-M., T.-Y.C., S.C.W. and M.F.Y. designed the experiments and wrote the manuscript. C.P.-M., T.-Y.C., B.K.K. and C.L.G. performed the experiments.

COMPETING FINANCIAL INTERESTS

The authors declare competing financial interests: details accompany the full-text HTML version of the paper at http://www.nature.com/naturemethods/.

Published online at http://www.nature.com/naturemethods/.
Reprints and permissions information is available online at http://npg.nature.com/reprintsandpermissions/.

1. Lieschke, G.J. & Currie, P.D. *Nat. Rev. Genet.* **8**, 353–367 (2007).
2. Zon, L.I. & Peterson, R.T. *Nat. Rev. Drug Discov.* **4**, 35–44 (2005).
3. Rubinstein, A.L. *Curr. Opin. Drug Discov. Dev.* **6**, 218–223 (2003).
4. McGrath, P. & Li, C. *Drug Discov. Today* **13**, 394–401 (2008).
5. Shin, J.T. & Fishman, M.C. *Annu. Rev. Genomics Hum. Genet.* **3**, 311–340 (2002).
6. Karlsson, J., Hofsten, J.V. & Olsson, P.E. *Mar. Biotechnol.* **3**, 522–527 (2001).
7. Gehrig, J. *et al. Nat. Methods* **6**, 911–916 (2009).
8. Rohde, C.B., Zeng, F., Gonzalez-Rubio, R., Angel, M. & Yanik, M.F. *Proc. Natl. Acad. Sci. USA* **104**, 13891–13895 (2007).
9. Funfak, A., Brosing, A., Brand, M. & Kohler, J.M. *Lab Chip* **7**, 1132–1138 (2007).
10. Buckley, C.E., Goldsmith, P. & Franklin, R.J.M. *Dis. Model. Mech.* **1**, 221–228 (2008).
11. Fricke, C., Lee, J.-S., Geiger-Rudolph, S., Bonhoeffer, F. & Chien, C.-B. *Science* **292**, 507–510 (2001).
12. Xiao, T., Roeser, T., Staub, W. & Baier, H. *Development* **132**, 2955–2967 (2005).
13. Steinmeyer, J.D. *et al. Nat. Protoc.* **5**, 395–407 (2010).
14. Bhatt, D.H., Otto, S.J., Depoister, B. & Fetcho, J.R. *Science* **305**, 254–258 (2004).
15. Yanik, M.F. *et al. Nature* **432**, 822 (2004).

ONLINE METHODS

High-throughput screening platform. The system can load larvae from reservoirs or multiwell plates (**Fig. 1**). The multiwell plate loading stage consists of three linear precision motors (RCA2; Intelligent Actuators). The motors are controlled by RACON 20/30 drivers (Intelligent Actuators). The loading head consists of a larva-loading and a water-supply metal tube with inner diameters of 1.0 and 0.2 mm, respectively (New England Small Tube) inserted into a silicone rubber block. The silicone rubber block is pressed (by the loading stage motor) against the top of the multiwell plate to seal the wells. One tube aspirates the larva from the sealed well, and the other tube injects water. Two fluidic valves (075P2NC12; Bio-Chem Fluidics) are used to switch the flow between the reservoirs and multiwell plate by pinching the silicone tubing (1/32 inch (0.8 mm) inner diameter × 3/32 inch outer diameter; Bio-Chem Fluidics). Larvae are driven through the system using a syringe pump (Carvo XLP6000; Tecan Systems). The photodetection system consisted of an integrated photodiode and an amplifier chip (OPT301; Texas Instruments) and two LEDs (Cree Inc) aligned in transmission and reflection configurations. The imaging system consists of a hybrid microscope capable of simultaneous upright and inverted imaging (Eclipse Ti, Nikon (inverted) and 90i Digital Imaging Head, Nikon (upright)) with two light sources (Mercury lamp; Nikon) (**Fig. 1**). The top port of the upright microscope was equipped with a multibeam laser confocal scanning head (Infinity 3; VisiTech) with a 1,004 × 1,002 pixel electron-multiplying charge-coupled device (CCD) camera (iXon+885; Andor Technology) for high-speed confocal imaging. For high-speed image sectioning, a piezo actuator with 400 µm travel distance (P-725 PIFOC; Physik Instrumente) holds either a 10× air lens (numerical aperture (NA) = 0.5) or 16× (NA = 0.8) (Nikon) or 20× (NA = 1.0) water-immersion lens (Olympus). A high-speed CCD camera (GX-1050; Prosilica) was connected to the inverted microscope equipped with 10× air objective lens for larva detection, positioning and rotation. Two precision stepping motors (KP35FM2-044; Japan Servo Co.) held a capillary of diameter 800 µm along its axis of rotation. The motors were controlled by a microstepping driver (BSD-02LH; Interinar Electronics). The motor and capillary assembly were mounted on a three-axis precision stage (MPC-200; Sutter Instrument) with 64-nm resolution along each axis. Two NIDAQ input-output data cards (PCI-6512 and PCI-6259; National Instruments) installed in a Dell OptiPlex computer controlled the fluidic valves, stepper motors and read out the voltage across the photodetector.

System automation. We provide a detailed algorithm for operation sequence of the system in a flowchart (**Supplementary Fig. 2**). The system starts by initializing syringe pumps, cameras, lamps, shutters, position stages and motors. The fluidic valves (**Fig. 1**) are switched to the source of fish, that is, either multiwell plate or fish reservoir. The larva is aspirated from the selected source at a constant rate of acceleration of 42 µl s^{-2} up to a maximum speed of 330 µl s^{-1}. The photodetector is continuously sampled at 2-kHz rate via the NIDAQ PCI-6259 card until the intensity reading crosses a predetermined threshold (the value of threshold is calibrated in advance by trial and error). Upon detection of the larva, the fluidic valve is switched to the water reservoir if the larva is being loaded from the fish reservoir. The aspiration rate is then decreased to 83 µl s^{-1} to avoid damaging the larva at the entrance of the capillary. The high-speed CCD at the bottom port continuously reads at 100 frames s^{-1}. The pixel intensity is averaged over the entire field of view and compared to a predetermined threshold (value of threshold is calibrated in advance by trial and error). When average pixel intensity drops below the threshold, the aspiration is stopped. The capillary is then rotated via the motors until the larva is at the desired orientation. A large-field-of-view image of the gross morphology of the larva is acquired by the CCD at the bottom port. The motorized shutter of the inverted microscope (bottom shutter) is closed while that of the upright microscope (top shutter) is opened. Image acquisition is switched from the bottom CCD to either the top CCD or the high-speed scanning confocal head equipped with the electron-multiplying CCD. Guided by fluorescence imaging, the region of interest is located. Either confocal stacks or widefield fluorescence images are acquired. The top shutter is closed, and the bottom shutter is opened. The image acquisition is switched to the bottom port. The system is now ready for the next cycle of operation. The control software is written in Matlab (Mathworks). The most recent version of the software is available upon request from the authors (M.F.Y.).

Animals. The fluorescent retinal ganglion line (*robo2*$^{ti272z/ti272z}$ (ast/ast) with *Tg(pou4f3:gap43-GFP)s356t*), the fluorescent lateral neuron line and the *Et(tol2:GFP) j1282b* were maintained and crossed using standard techniques. All animal experiments were approved by MIT's Committee on Animal Care under protocol 0309-025-12.

Axon guidance screen. Genotypically homozygous *robo2*$^{+/+}$ (+/+) and *robo2*$^{ti272z/ti272z}$ (ast/ast) fish were crossed to generate heterozygous *robo2*$^{ti272z/+}$ (ast/+) larvae. A 96-well plate was randomly and partially populated with the heterozygous ast/+ progeny. The rest of the wells were populated with the homozygous progeny of ast/ast fish. A screen was performed in a blinded fashion by loading the zebrafish from multiwell plates and orienting them to visualize midline crossing as in **Figure 2a** by a 10× (NA = 0.5) objective lens with long depth of focus in widefield fluorescence imaging mode. Zebrafish were classified in a blinded fashion according to the observed phenotype.

Laser axotomy. A tunable femtosecond laser (Mai Tai; Spectra-Physics Lasers) was guided to the upright microscope for laser axotomy as we previously described[13]. The axon fiber of enhanced GFP (EGFP)-expressing lateral neuron was cut 850 µm from the soma using ultrashort laser pulses with 780 nm wavelength, 100 fs duration, 12.7 nJ pulse energy, 80 MHz repetition rate and 10 ms long pulse train focused by a 20× (NA = 1.0) objective lens. Statistics of laser cut sizes were quantified with a 40× (NA = 0.8) objective lens. Surgeries were repeated on 30 zebrafish with 100% success rate.

Assessment of zebrafish health. The syringe was operated at three different initial aspiration rates of 165, 250 and 330 µl s^{-1} for loading 2-d.p.f. larvae from multiwell plates. In total, 450 larvae were anesthetized with 0.20 mg ml^{-1} tricaine, loaded and dispensed from the platform. A control group of 150 larvae from the same breed were similarly anesthetized. Health assessment was based on both functional and morphological criteria measured

doi:10.1038/nmeth.1481

at 0, 12, 16, 20, 24, 28, 32 and 36 h after screening. Functional criteria included visual confirmation of normal heartbeat and reflex response to touch stimuli. Morphology criteria included bending (that is, lordosis, kyphosis and scoliosis) and craniofacial abnormalities. Abnormalities were counted even if the zebrafish regenerated later.